How to cite: *Angew. Chem. Int. Ed.* **2024**, *63*, e202317343
doi.org/10.1002/anie.202317343

Heterogeneous Catalysis

Pt/MnO Interface Induced Defects for High Reverse Water Gas Shift Activity

Imre Szenti, Anastasiia Efremova, János Kiss, András Sápi, László Óvári, Gyula Halasi, Ulrich Haselmann, Zaoli Zhang, Jordi Morales-Vidal, Kornélia Baán, Ákos Kukovecz, Núria López, and Zoltán Kónya*

Abstract: The implementation of supported metal catalysts heavily relies on the synergistic interactions between metal nanoparticles and the material they are dispersed on. It is clear that interfacial perimeter sites have outstanding skills for turning catalytic reactions over, however, high activity and selectivity of the designed interface-induced metal distortion can also obtain catalysts for the most crucial industrial processes as evidenced in this paper. Herein, the beneficial synergy established between designed Pt nanoparticles and MnO in the course of the reverse water gas shift (RWGS) reaction resulted in a Pt/MnO catalyst having ≈10 times higher activity compared to the reference Pt/SBA-15 catalyst with >99 % CO selectivity. Under activation, a crystal assembly through the metallic Pt (110) and MnO evolved, where the plane distance differences caused a mismatched-row structure in softer Pt nanoparticles, which was identified by microscopic and surface-sensitive spectroscopic characterizations combined with density functional theory simulations. The generated edge dislocations caused the Pt lattice expansion which led to the weakening of the Pt–CO bond. Even though MnO also exhibited an adverse effect on Pt by lowering the number of exposed metal sites, rapid desorption of the linearly adsorbed CO species governed the performance of the Pt/MnO in the RWGS.

Introduction

The global challenge of excessive CO_2 release into the atmosphere necessitates catalysis as a pivotal solution for its efficient utilization, which can partially replace traditional exhaustible carbon sources, such as oil and gas.[1,2] Interfaces in catalyst systems have long been recognized as the most critical factor in controlling catalytic reaction mechanisms.[3] In supported catalysts, the metal-support interactions (MSI) may induce electronic alterations;[4,5] affect the shape of the nanoparticles;[6,7] or bring about the metal nanoparticles coverage by support suboxides during reductive treatment, which is often referred to as strong metal-support interaction (SMSI).[8,9] The unique structure of the interface and its electronic, geometric, and energetic consequences govern the activity, selectivity, and stability of a heterogeneous catalyst in various reactive processes. Thus, developing highly active catalysts with appropriate interfacial synergy is crucial for enabling decarbonization and de-fossilization technologies.

Syngas, obtained through reverse water gas shift reaction (RWGS) combined with the Fischer–Tropsch process offers a promising possibility for sustainable energy development.[10] Being a net carbon consuming process, RWGS is superior to other syngas production methods in mitigating the CO_2 emissions.[11] With the development of more affordable green hydrogen production technologies, RWGS is expected to become increasingly profitable as

[*] Dr. I. Szenti, A. Efremova, Dr. J. Kiss, Dr. A. Sápi, Dr. G. Halasi, K. Baán, Dr. Á. Kukovecz, Prof. Dr. Z. Kónya
Department of Applied and Environmental Chemistry, University of Szeged, Interdisciplinary Excellence Centre
Rerrich Béla tér 1, 6720 Szeged (Hungary)
E-mail: sapia@chem.u-szeged.hu

Dr. I. Szenti, Dr. J. Kiss, Dr. L. Óvári, Prof. Dr. Z. Kónya
HUN-REN-SZTE Reaction Kinetics and Surface Chemistry Research Group Institution
Rerrich Béla tér 1, 6720 Szeged (Hungary)

Dr. L. Óvári, Dr. G. Halasi
Extreme Light Infrastructure-ALPS, ELI-HU Non-Profit Ltd.
Wolfgang Sandner utca 3, 6728 Szeged (Hungary)

Dr. U. Haselmann, Dr. Z. Zhang
Erich Schmid Institute of Materials Science, Austrian Academy of Sciences
8700 Leoben (Austria)

J. Morales-Vidal, Prof. N. López
Institute of Chemical Research of Catalonia (ICIQ-CERCA), The Barcelona Institute of Science and Technology
Avinguda Països Catalans 16, 43007 Tarragona (Spain)

J. Morales-Vidal
Universitat Rovira i Virgili
Avingua Catalunya 35, 43002 Tarragona (Spain)

well.[12] It is imperative, nonetheless, that RWGS catalysts exhibit maximum CO selectivity at low temperatures (573–773 K).[13]

To meet these requirements, current research focus is shifted towards rational catalyst design for RWGS. One such approach is utilizing single-atom supported catalysts, which not only allows to achieve great activity but also maximizes the metal use.[14,15] Another popular approach implies utilization of dual support materials[16,17] to influence physicochemical properties of the supports towards better selectivity.

It was recently reported that adding MnO_x to the Cu-based catalyst promotes the activity and governs the CO selectivity by the generation of the Mn(II)-O-CO_2 surface complex, which suppresses further hydrogenation and favors CO desorption.[18] Moreover, excellent activity and high CO selectivity of Pt/ mesoporous MnO_2 system in the RWGS reaction have been recognized previously by our group,[19] however, a detailed understanding of the surface processes responsible for that activity enhancement is missing.

In this work, a novel type of metal-support interaction that evolved between size-controlled Pt (≈5 nm) nanoparticles and MnO is reported. The efficient synergy of the Pt/MnO allowed to achieve 10x-fold catalytic enhancement compared to the reference Pt/SBA-15 catalyst retaining maximum CO selectivity in the RWGS reaction. A combination of surface-sensitive spectroscopic [in situ diffuse reflectance infrared Fourier transform spectroscopy (DRIFTS); near ambient pressure X-ray photoelectron spectroscopy (NAP-XPS)] and microscopic (HR-TEM) techniques with density functional theory (DFT) simulations was applied to identify, characterize, and locate two types of linearly adsorbed carbon monoxide surface species. The facilitated desorption of linearly adsorbed CO is shown to be the key factor responsible for the improved activity over the Pt/MnO.

Results and Discussion

Metal-Support Interaction in the Pt/MnO

The as-prepared mesoporous MnO_2 demonstrated a rod-shaped morphology with a rod diameter of ~5–10 nm and a length of several hundred of nm. The XRD and electron diffraction (ED) characterization indicated that it can be classified as a β-type MnO_2 (JCPDS PDF# 24-0735), which is in agreement with other studies[20] (Figure S1a). Neither the morphology nor the crystallographic form of MnO_2 was altered after 0.5 % Pt nanoparticle loading. TEM image shows inhomogeneous Pt particle distribution with well-dispersed Pt particles in a range of ~5 nm in size. In the case of Pt/MnO_2, only the XRD peaks assignable to the tetragonal phase of β-MnO_2 were detected; Pt reflections were not identified due to low loading of the nanoparticles[21] (Figure S1b).

Before the catalytic experiments, all catalysts were activated by heat treatment in oxidative (573 K, 30 min) and subsequent reductive (673 K, 60 min) atmospheres. Therefore, the characterization of the catalysts after the pre-treatment is more relevant. As a result of the pre-treatment process, the mesostructure of the MnO_2 collapsed (Figure S2a), which led to a significant decrease in the sorption capacity (Table S1). From the XRD pattern, reflections attributed to the spinel structure of Mn_3O_4 (JCPDS PDF# 24-0734) were found to coexist with the reflections of MnO crystalline phase (JCPDS PDF# 78-0424). These results are complemented by the ED analysis data (Figure S2a). The reducibility of the support was studied by H_2-temperature programmed reduction (H_2-TPR). The MnO_2 displays two reduction peaks at 540 and 630 K with a total H_2 consumption of 6.8 mmol g^{-1} (Figure S2b). The lower temperature reduction peak can be ascribed to the reduction of MnO_2 to Mn_3O_4 and the peak at the higher temperature is due to the reduction of Mn_3O_4 to MnO.[22]

To investigate the surface state of Mn species after the pre-treatment, NAP-XPS was implemented. Details of the peak assignment and fitting can be found in the SI. The Mn 2p main peaks and the separation between the satellite and the Mn $2p_{1/2}$ peak (10.5 eV), strongly suggest the reduction of Mn^{4+} to Mn^{3+} (Figure S2c). The separation between the peaks in the Mn 3 s region (5.6 eV) indicates a mixture of Mn^{2+} and Mn^{3+} (Figure S2d). To estimate the quantity of manganese with different oxidation states, peak fitting of the Mn 3 s region was performed (Figure S3e). The fitting confirmed that MnO_2 was essentially reduced to Mn^{3+}, with the minor presence of Mn^{2+} (3 % of the total Mn content), therefore, the MnO_x nomenclature is introduced to refer to the reduced MnO_2.

With regards to the Pt-supported sample, MnO_2 was fully reduced to MnO. No significant sintering or aggregation of Pt nanoparticles was observed after the activation process (Figure 1a). The facilitated reduction after Pt incorporation was also supported by the H_2-TPR results. In contrast to the pure support, one intense reduction peak at 447 K was observed showing that a large part of MnO_2 is reduced at a lower temperature due to the spillover effect.[19] This is also consistent with the decreased intensity of the peak at 530 K (Figure 1b). CO_2-TPD analysis was applied to

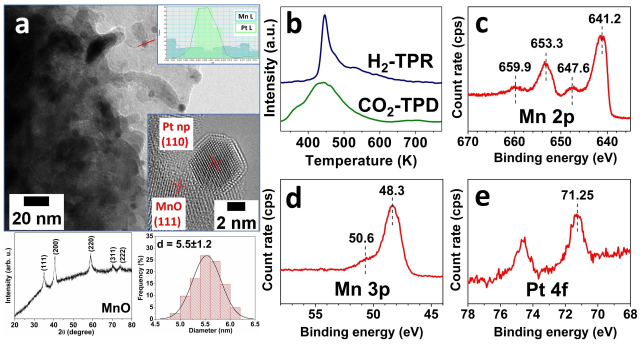

Figure 1. Characterization of the Pt/MnO catalyst after activation: a) TEM image, X-Ray diffraction pattern and Pt distribution histogram. b) H_2-TPR and CO_2-TPD profiles. c) Mn 2p; d) Mn 3p; e) Pt 4f XPS regions. Inset: a) HAADF STEM image with corresponding EDS signal and HR-TEM image of the activated Pt/MnO.

determine the catalyst's relative basicity. The basic concentration remained the same and no considerable shift in the peak positions was observed when Pt nanoparticles were loaded, compared to the pure support (Figure S2b, 1b). Thus, the incorporation of Pt nanoparticles does not have any effect on the catalyst basicity, in contrast to our previous findings on mesoporous cobalt oxide.[21]

The NAP-XP spectrum of the Pt-containing sample collected after the oxidation-reduction pre-treatment showed that in the Mn 2p region, $2p_{3/2}$ component at 641.2 eV and the $2p_{1/2}$ component at 653.3 eV dominated (Figure 1c). Besides, shake-up satellites were observed at a distance of ≈6.5 eV from the main peaks. This complex line shape is a clear signature of Mn^{2+}. Importantly, the well-known shake up satellites, attributable to Mn^{3+} and Mn^{4+} were completely missing. The Mn 3p region was in harmony with this conclusion, the observed peak position (48.3 eV), and the asymmetry towards higher binding energies are characteristic of MnO[23,24] (Figure 1d). Regarding the Pt 4f region, the Pt $4f_{7/2}$ component appeared at 71.25 eV, which is characteristic of metallic platinum[25–27] (Figure 1e). Hence, the working state of the catalyst is Pt/MnO, and this designation will be followed onward.

The catalytic activity of supported metal catalysts directly depends on the exposed surface area per volume of the metal component. The number of available metal sites was assessed in terms of Pt dispersion (D,%). To evaluate the extent of metal-support interactions established in the Pt/MnO, the results were compared to the reference catalyst —0.5 % 5 nm Pt nanoparticles supported mesoporous silica (SBA-15) (Figure S3). Silica is generally considered to be inert, therefore, weak metal-support interactions are expected in the Pt/SBA-15 system. The actual metal loading determined by ICP-MS was very close to the nominal value and a small increase in Pt nanoparticle size after the pre-treatment was characteristic for both catalysts (Table S2). The O_2–H_2-pulse titration results indicated 47.4 % of metal dispersion in the case of Pt/SBA-15, which is comparable to the value obtained on similarly sized Pt-nanoparticles supported on an inert material after the PVP removal procedure.[28] This verifies the PVP removal efficiency of the oxidative treatment applied in the current work.

Interestingly, much lower dispersion was measured for the Pt/MnO (10.5 %), suggesting that the major part of Pt atoms is inaccessible for the adsorption (Table S2).

Effect of the Metal-Support Interaction in the RWGS

The MnO_x and Pt/MnO catalysts were tested in RWGS reaction. The Pt/MnO exhibited considerably higher catalytic activity compared to the pure support. However, since the pure support and the Pt-loaded catalysts contain manganese in different valence state, comparison of their catalytic activity is inadequate. In this regard, catalytic measurements under identical reaction conditions were performed over commercial MnO purchased from Aldrich (MnO) (Figure 2a). The results revealed that pure MnO is inactive in converting CO_2. Notable catalytic performance

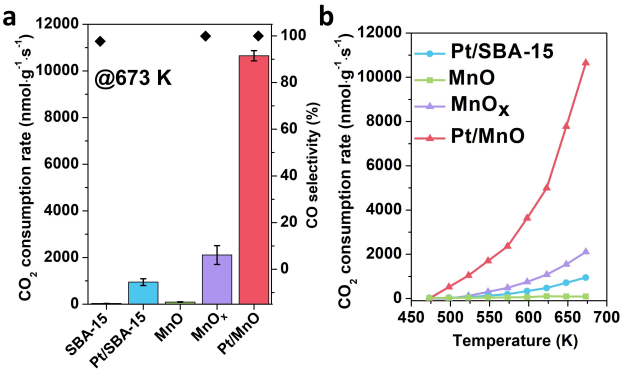

Figure 2. CO_2 consumption rate in the RWGS reaction over a) MnO, MnO_x, Pt/MnO at 673 K where pure SBA-15 and Pt/SBA-15 are represented as reference state catalysts. b) CO_2 consumption rate for MnO, MnO_x, Pt/MnO, and Pt/SBA-15 in the heating phase. Reaction conditions: $CO_2:H_2=1:4$; GHSV = 16000 $mL\cdot g^{-1}\cdot h^{-1}$.

can be achieved exclusively in the presence of Pt, which is clear evidence of the beneficial synergy between Pt and MnO. The enhancement effect of 5 nm Pt nanoparticles on the MnO was also compared to the reference Pt/SBA-15 catalyst which showed little turnover in the CO_2 hydrogenation. Naturally, the CO_2 consumption rate greatly increased on elevating the reaction temperature (Figure 2b). At the same time, no selectivity changes were observed: both MnO_x and Pt/MnO exhibited ≈100 % CO selectivity at 673 K.

Reducible supports that are most commonly utilized for the RWGS process are titania and ceria. For that reason, we have prepared mesoporous TiO_2 and CeO_2 through the same synthesis procedure and tested their 0.5 % 5 nm Pt nanoparticle-loaded counterparts in the RWGS under identical reaction conditions. The comparison of catalytic performance between investigated catalysts and the reported efficient catalysts are summarized in Table S3. These results demonstrate that RWGS activity is significantly enhanced over Pt/MnO catalyst compared to Pt/CeO_2 and Pt/TiO_2, which further confirms that beneficial synergy established between MnO and Pt nanoparticles. Naturally, there are ways to optimize Pt/CeO_2 and Pt/TiO_2 systems towards more elevated catalytic performance by decreasing the Pt size[29] or modifying the support.[30] The primary hurdle for the Pt/MnO system to demonstrate comparable catalytic activity can be attributed to the greatly diminished number of exposed metal sites (Table S2).

Kinetic parameters such as activation energy and reaction order with respect to CO_2 were determined for the Pt/MnO in comparison with the Pt/SBA-15 catalyst and summarized in Figure S4. In the case of Pt/MnO, the higher apparent activation energy for CO (45.6 ± 2.8 $kJ\cdot mol^{-1}$) may be originated from a geometric effect caused by MnO species on the Pt surface, as evidenced by low metal dispersion (Table S2).[31] The apparent reaction order in the CO_2 pressure was 0.75 for Pt/MnO, which is in good agreement with the Pt/TiO_2 catalyst (0.79 at 623 K).[32] In the case of Pt/SBA-15, a decrease in the reaction order

compared to the Pt/MnO (0.57) may suggest that the active sites are poisoned by the main product of the RWGS reaction[33] (Figure S4b).

To determine whether the chemical state of the surface layer has changed in the course of the RWGS over Pt/MnO, NAP-XPS characterization of the spent sample was carried out. The XPS spectrum recorded in the H_2+CO_2 mixture at 673 K was very similar in each studied region compared to that collected after the pre-treatment (Figure S5). The C 1s region did not show any significant accumulation of carbon (not shown). In the bulk of the catalyst, reflections assignable to the MnO phase were registered as shown in the XRD of spent catalyst (Figure S5).

The adsorbed species formed on the surface of the Pt/MnO in the presence of the reactant mixture/products at 673 K were comparatively studied to obtain a molecular-level understanding of the superior performance of Pt/MnO in the CO_2 hydrogenation (Figure 3a). It should be noted that the denoted wavenumbers may vary by $\pm 5\ cm^{-1}$ within one data set as a function of temperature.

In both cases, the formation of the gas phase products—methane and CO—were detectable at $3016\ cm^{-1}$ and at $\approx 2200\ cm^{-1}$ (not shown) from 600 K.[34]

For the MnO catalyst, the three strongest bands at 1552, 1323 and $1059\ cm^{-1}$ are attributable to bidentate carbonate species, which appeared on several oxides.[35,36] The band at $1434\ cm^{-1}$ may be assigned to polydentate carbonate.[35]

In the case of Pt/MnO, broad overlapping bands were observed in the spectral region from ≈ 1300 to $1600\ cm^{-1}$. The analysis of the deconvoluted spectra (Figure 3a inset) allowed to separate infrared vibrations of the bidentate carbonate species registered at 1549 and $1318\ cm^{-1}$ from two new unassigned bands. These peaks may belong to the adsorbed formate (HCOO) species—one of the most evident species arising from CO_2 hydrogenation and related works on metal-supported oxides. They are characterized by a very strong absorption band at 1600–1550 cm^{-1} and another weaker split at 1400–1350 cm^{-1}.[37,38] A distinctive C–H stretch of the formate species registered on the Pt/MnO at $2831\ cm^{-1}$ further supports this affirmation.[39]

Another significant difference between the spectral features of MnO and Pt/MnO catalysts can be easily recognized: adsorbed CO is detectable at $2024\ cm^{-1}$ on the Pt containing sample. It may form as the result of formate species decomposition:[40]

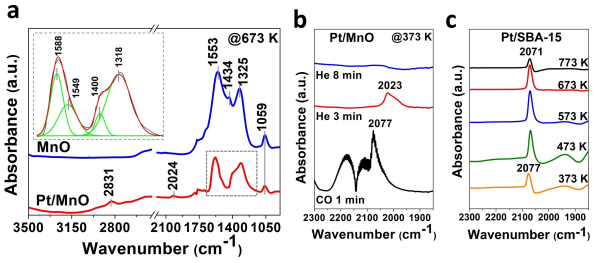

Figure 3. DRIFT spectra recorded during a) CO_2+H_2 reaction at 673 K over MnO and Pt/MnO. b) CO adsorption at 373 K on Pt/MnO. c) CO TPD over Pt/SBA-15.

$$HCOO_{(a)} \rightarrow CO_{(a)} + OH_{(a)} \rightarrow CO_{(g)} + H_2O_{(g)}.$$

It is interesting that the CO band observed under the reaction conditions appeared at a significantly lower wavenumber. Linearly adsorbed CO stretching on the atop site of the Pt surface is normally registered at $\approx$2070–2080 cm^{-1} depending on the nature of the support.[21,41,42] The CO adsorption and the corresponding frequencies were computed in several sites of Pt/MnO models (Figure S6). However, most conformations were discarded to represent the experimental results due to unfavored adsorption energies or too low CO frequencies.

In order to experimentally study the adsorption behavior of carbon monoxide in the case of Pt/MnO, carbon monoxide was introduced to the surface of the catalyst at 373 K. When the CO coverage was still high, gaseous CO twin band with peak maxima at 2170 and $2115\ cm^{-1}$ can be registered and an asymmetric band due to the linearly bonded CO appeared at a conventional wavenumber—$2077\ cm^{-1}$ (Figure 3b). After 3 minutes in helium at 373 K, this band vanished completely, and the adsorbed CO observed under the reaction conditions was detectable at $2023\ cm^{-1}$ which also disappeared promptly after a short helium flush. It is remarkable how adsorbed carbon monoxide is highly unstable on the Pt/MnO. In contrast, adsorbed CO ($2077\ cm^{-1}$) was distinguished with an excellent stability (up to 773 K) as revealed from the CO-TPD on the reference Pt/SBA-15 catalyst (Figure 3c).

Origin of the enhancement effect in Pt/MnO

In this study, it was demonstrated that the addition of Pt nanoparticles promotes RWGS reaction over MnO. This can be attributed to the generation of new active sites since platinum has very well-established catalytic properties. However, from Figure 2a it is apparent that the Pt enhancement effect on mostly inert silica is far inferior to that on the MnO support.

In catalytic systems, support defects such as oxygen vacancies can play a very important role by activating the CO_2 molecule. The existence of interstitial oxygen deficiencies within the lattice of the MnO implies the presence of reduced manganese, however, no significant change was observed in the XPS Mn2p spectra (Figure 1c, S5c). Therefore, oxygen vacancies in MnO have no detectable effect on the RWGS activity of the Pt/MnO.

Herein, the most significant experimental findings observed exclusively in the case of Pt/MnO were the reduced metal dispersion and the low-frequency adsorbed CO species, which may be ascribed to the improved activity.

Suppressed chemisorption capacity and low metal dispersion are generally characteristic for SMSI, during which a reducible oxide support forms an overlayer on the surface of a metal particle.[43] In this process, an electron transfer from partially reduced support to metal nanoparticles is initiated, which can be reflected in red-shift of the adsorbed CO wavenumber.[44] In our case, NAP-XPS results indicate no

electron transfer since the observed Pt 4f binding energy coincides with the value expected for bulk platinum.[45] Moreover, the information about electronic interactions between Pt and Mn^{2+} was obtained through Ultraviolet Photoelectron Spectroscopy (UPS) measurements which were carried out over MnO and Pt/MnO samples. No considerable change in the work function was observed with Pt nanoparticle loading, therefore, it was concluded that there is no significant electron transfer between Pt and Mn^{2+}. On the other hand, without an electron transfer, partial encapsulation is not likely to be responsible for the weakening of the Pt–CO bond.

Considering other factors, the observed decrease in the vibrational C–O frequency first and foremost may originate from low-coordinated small platinum nanoparticles.[46] It has long been discovered that decreasing the Pt nanoparticle size to a single atom not only exploits less valuable material but also brings about great improvements in the catalytic activity especially in the CO_2 reduction.[47] It has been frequently observed that the binding energy for small metallic clusters is shifted to higher values compared to the bulk phase, attributed mostly to less efficient screening of the core hole in small clusters.[25,48] The absence of this phenomenon here indicates that the metal nanoparticles are not particularly small as evidenced from TEM (Figure 1a). Furthermore, there was no appreciable change in the Pt 4f/Mn 2p area ratio either, indicating no considerable changes in the particle size of Pt as an effect of the reacting gas mixture.

Therefore, the Pt-MnO favorable interfacial attachment remains the only factor attributable to the observed activity enhancement. Lee et al.[49] have also drawn this conclusion in the study of MnO_x/Pt/γ-Al_2O_3 layered catalyst in the CO oxidation reaction, however, no straightforward explanation for the beneficial effect of this interfacial contact in the CO oxidation could be provided.

To gain a more detailed understanding of the catalysts' atomic-level structure, HR-TEM and associated techniques were employed. Analyzing the HR-TEM images of Pt/MnO after the RWGS reaction, an atomic interface of Pt particle and MnO could be observed provided that both Pt and MnO were in the right zone axis. Clear edge dislocations were detected at the Pt-MnO interface (Figure 4a,b). Such crystal defects are proposed to form during the pre-treatment process via imperfect attachment of Pt and MnO crystal planes (the Pt-MnO lattice misfit comprises around 12 %) in which MnO planes contract and Pt planes expand (Figure 4c). This observation was not coincidental and was also detected for other Pt nanoparticles-MnO interfaces (Figure S7).

In general, defects created on conventional catalysts can impact the adsorption behavior of reactants or intermediates, which can assist in the transformation of the intermediates into products.[50] Thus, it was shown that the expansion in the Pt lattice may cause the weakening of the Pt–CO bond due to the reduced π back-donation from Pt to CO.[51]

In order to establish whether the connection between the observed edge dislocations and low-frequency CO is indeed relevant, DFT simulations were carried out. Modelling the lattice mismatch structure appears to be quite cumbersome. Therefore, the CO adsorption on the Pt nanoparticle deposited on MnO (100) with one Pt vacancy in the interface was computed. This model mimics the edge dislocation at the Pt/MnO interface, where Pt d-spacing is expanded (Figure 4d). DFT results showed that the presence of Pt vacancy causes CO stretching frequency to decrease by 41 cm^{-1}. Interestingly, the calculated CO stretching on the defect site (2023 cm^{-1}) agrees well with the experimental observation (2023–2024 cm^{-1}).

As evidenced by DRIFTS data, there are two types of adsorption sites on platinum available for carbon monoxide. The low-frequency CO species registered at 2024 cm^{-1} are adsorbed on Pt atoms close to the mismatched row interfacial sites as revealed by the computational results while the adsorbed CO on defect-free Pt was detected at the regular wavenumber—2077 cm^{-1}. Both species are attributed to the linearly adsorbed CO and were revealed to desorb at a very low temperature (373 K) from the surface (Figure 3b). The enhanced desorption of the CO species is the consequence of the distortion of Pt nanoparticles by the edge dislocations at the Pt/MnO interface. Even though the coverage of Pt nanoparticles by the MnO greatly hindered the Pt adsorption capacity, it is the fast release of the linearly adsorbed carbon monoxide species from the surface that is proposed to govern the activity of Pt/MnO in the RWGS reaction.

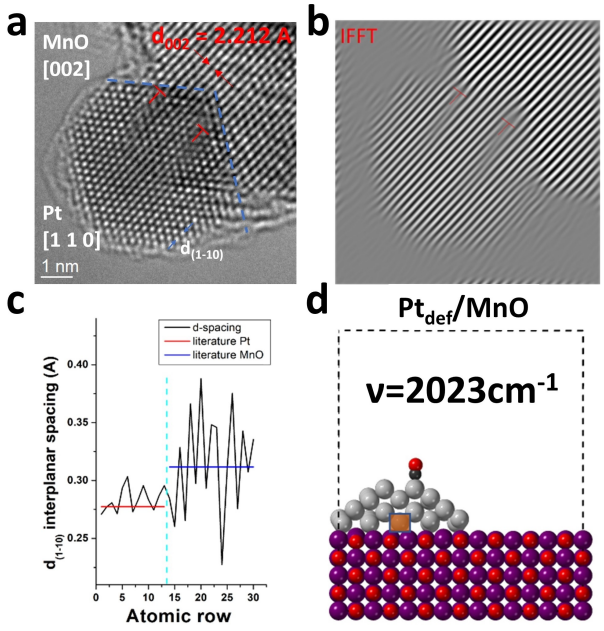

Figure 4. a) HR-TEM image evidencing on edge dislocations at the Pt-MnO interface. b) IFFT of the HR-TEM image. c) Interplanar spacing of Pt and MnO. d) Computed CO vibrational frequency (ν) on a model of Pt nanoparticle with one Pt vacancy in the interface with MnO (Pt_{def}/MnO). Colour code: Mn (purple), O (red), Pt (grey), C (dark grey), Pt vacancy (orange), and unit cell (dashed black line).

Conclusion

In this study, size-controlled Pt nanoparticles were prepared by the polyol method and anchored onto mesoporous manganese dioxide. The support reduction was facilitated by Pt nanoparticles loading due to the H_2-spillover effect and resulted in the presence of mostly Mn^{2+} on the surface after the activation process while the bare support contained oxidized manganese in the form of Mn^{3+}. The Pt/MnO catalyst showed enhanced performance in the RWGS: the CO_2 consumption rate was $\approx$10 times higher compared to the reference Pt/SBA-15 catalyst at 673 K with an excellent CO selectivity.

A complex controversial synergy emerged between Pt nanoparticles and MnO, the origin of which was successfully unraveled with the help of chemisorption measurements, in situ, microscopic and computational techniques. On the one hand, MnO species imposed a geometric impact on Pt as the result of strong metal-support interaction. Thus, the number of available Pt metal sites was considerably reduced compared to the Pt/SBA-15 catalyst (Table S2). On the other hand, edge dislocations were generated at the Pt/MnO interface, the formation of which was manifested in the decrease of the linearly adsorbed CO frequency (2024 cm^{-1}) (Figure 4). The adsorbed CO on defect-free Pt was also observed at 2077 cm^{-1}, however, independently of the location, the adsorbed CO species, formed as the result of formate species decomposition, were greatly destabilized on the Pt surface (Figure 3b). The destabilization was assigned to the weakening of the Pt–CO bond due to the Pt lattice expansion in the course of mismatched-row structure formation. The accelerated desorption of linearly adsorbed CO is proposed to be responsible for the improved catalytic performance of the Pt/MnO in the RWGS. As a future outlook, strategies to fully unlock the catalytic potential of Pt/MnO by modulating SMSI can be developed. Our work demonstrates the importance of atomic-level insights in establishing the synergy effect consequences in supported metal catalysts. The design of efficient catalysts with appropriate synergistic interactions could potentially reduce the demand for critical materials in future applications.

Acknowledgements

AS gratefully acknowledges the support of FK 143583 and ZK is grateful for K 21 138714 and SNN_135918 project from the source of the National Research, Development and Innovation Fund. The Ministry of Human Capacities through the 20391-3/2018/FEKUSTRAT, as well as Project no. TKP2021-NVA-19 under the TKP2021-NVA funding scheme of the Ministry for Innovation and Technology are acknowledged. Project no. RRF-2.3.1-21-2022-00009, titled National Laboratory for Renewable Energy has been implemented with the support provided by the Recovery and Resilience Facility of the European Union within the framework of Programme Széchenyi Plan Plus. The Spanish Ministry of Science and Innovation is acknowledged for financial support (PRE2019-088791, PID2021-122516OB-I00, and Severo Ochoa Grant MCIN/AEI/10.13039/501100011033 CEX2019-000925-S) and the Barcelona Supercomputing Center-MareNostrum (BSC-RES) for providing generous computer resources.

Conflict of Interest

The authors declare no conflict of interest.

Data Availability Statement

The data that support the findings of this study are available in the supplementary material of this article.

Keywords: Edge Dislocations · Low CO Stability · Manganese Oxide · Pt/Mno Interface · RWGS

[1] M. González-Castaño, B. Dorneanu, H. Arellano-García, *React. Chem. Eng.* **2021**, *6*, 954–976.
[2] L. Jeffry, M. Y. Ong, S. Nomanbhay, M. Mofijur, M. Mubashir, P. L. Show, *Fuel* **2021**, *301*, 121017.
[3] W. Gao, Z. D. Hood, M. Chi, *Acc. Chem. Res.* **2017**, *50*, 787–795.
[4] D. E. Resasco, G. L. Haller, *J. Catal.* **1983**, *82*, 279–288.
[5] Y. Lykhach, S. M. Kozlov, T. Skála, A. Tovt, V. Stetsovych, N. Tsud, F. Dvořák, V. Johánek, A. Neitzel, J. Mysliveček, S. Fabris, V. Matolín, K. M. Neyman, J. Libuda, *Nat. Mater.* **2016**, *15*, 284–288.
[6] I. Lee, R. Morales, M. A. Albiter, F. Zaera, *Proc. Natl. Acad. Sci. USA* **2008**, *105*, 15241–15246.
[7] T. Sakpal, L. Lefferts, *J. Catal.* **2018**, *367*, 171–180.
[8] T. W. van Deelen, C. Hernández Mejía, K. P. de Jong, *Nat. Catal.* **2019**, *2*, 955–970.
[9] J. Li, Y. Lin, X. Pan, D. Miao, D. Ding, Y. Cui, J. Dong, X. Bao, *ACS Catal.* **2019**, *9*, 6342–6348.
[10] J. Guilera, J. A. Díaz-López, A. Berenguer, M. Biset-Peiró, T. Andreu, *Appl. Catal. A* **2022**, *629*, 118423.
[11] E. Rezaei, S. Dzuryk, *Chem. Eng. Res. Des.* **2019**, *144*, 354–369.
[12] R. M. Bown, M. Joyce, Q. Zhang, T. R. Reina, M. S. Duyar, *Energy Technol.* **2021**, *9*, 28–31.
[13] G. Sun, S. Mottaghi-Tabar, L. Ricardez-Sandoval, D. S. A. Simakov, *Top. Catal.* **2021**, *64*, 414–430.
[14] L. Chen, R. R. Unocic, A. S. Hoffman, J. Hong, A. H. Braga, Z. Bao, S. R. Bare, J. Szanyi, *JACS Au* **2021**, *1*, 977–986.
[15] W. Zhang, A. Vidal-López, A. Comas-Vives, *Front. Chem.* **2023**, *11*, 1144189.
[16] J. Wu, Y. Zheng, J. Fu, Y. Guo, J. Yu, J. Chu, P. Huang, C. Zhao, *Sep. Purif. Technol.* **2023**, *317*, 123916.
[17] A. Ranjbar, S. F. Aghamiri, A. Irankhah, *Int. J. Hydrogen Energy* **2023**, *48*, 19115–19125.
[18] R. Dalebout, L. Barberis, N. L. Visser, J. E. S. van der Hoeven, A. M. J. van der Eerden, J. A. Stewart, F. Meirer, K. P. de Jong, P. E. de Jongh, *ChemCatChem* **2022**, *14*, e202200451.
[19] A. Sápi, T. Rajkumar, M. Ábel, A. Efremova, A. Grósz, A. Gyuris, K. B. Ábrahámné, I. Szenti, J. Kiss, T. Varga, Á. Kukovecz, Z. Kónya, *J. CO2 Util.* **2019**, *32*, 106–118.
[20] S. M. Lee, H. Eom, S. S. Kim, *Environ. Technol.* **2021**, *42*, 182–192.
[21] A. Efremova, I. Szenti, J. Kiss, Á. Szamosvölgyi, A. Sápi, K. Baán, L. Olivi, G. Varga, Z. Fogarassy, B. Pécz, Á. Kukovecz, Z. Kónya, *Appl. Surf. Sci.* **2022**, *571*, 151326.

[22] J. Ye, M. Zhou, Y. Le, B. Cheng, J. Yu, *Appl. Catal. B* **2020**, *267*, 118689.
[23] G. C. Allen, S. J. Harris, J. A. Jutson, J. M. Dyke, *Appl. Surf. Sci.* **1989**, *37*, 111–134.
[24] B. D. Hermsmeier, C. S. Fadley, B. Sinkovic, M. O. Krause, J. Jimenez-Mier, P. Gerard, T. A. Carlson, *Phys. Rev. B* **1993**, *48*, 12425–12437.
[25] H.-P. Steinrück, F. Pesty, L. Zhang, T. E. Madey, *Phys. Rev. B* **1995**, *51*, 2427–2439.
[26] F. Pesty, H.-P. Steinrück, T. E. Madey, *Surf. Sci.* **1995**, *339*, 83–95.
[27] S. Krick Calderón, M. Grabau, L. Óvári, B. Kress, H.-P. Steinrück, C. Papp, *J. Chem. Phys.* **2016**, *144*, 044706.
[28] D. Romero, F. Oropeza, M. Rigutto, E. J. M. Hensen, *Fuel* **2022**, *317*, 123506.
[29] Z. Zhao, M. Wang, P. Ma, Y. Zheng, J. Chen, H. Li, X. Zhang, K. Zheng, Q. Kuang, Z. X. Xie, *Appl. Catal. B* **2021**, *291*, 120101.
[30] Z. Chen, L. Liang, H. Yuan, H. Liu, P. Wu, M. Fu, J. Wu, P. Chen, Y. Qiu, D. Ye, L. Chen, *Appl. Catal. B* **2021**, *298*, 120507.
[31] M. C. J. Bradford, A. M. Vennice, *J. Catal.* **1998**, *173*, 157–171.
[32] S. S. Kim, H. H. Lee, S. C. Hong, *Appl. Catal. A* **2012**, *423–424*, 100–107.
[33] G. D. Weatherbee, C. H. Bartholomew, *J. Catal.* **1982**, *77*, 460–472.
[34] J. Baltrusaitis, J. Schuttlefield, E. Zeitler, V. H. Grassian, *Chem. Eng. J.* **2011**, *170*, 471–481.
[35] Y. Guo, S. Mei, K. Yuan, D. J. Wang, H. C. Liu, C. H. Yan, Y. W. Zhang, *ACS Catal.* **2018**, *8*, 6203–6215.
[36] W. Taifan, J. Boily, J. Baltrusaitis, *Surf. Sci. Rep.* **2016**, *71*, 595–671.
[37] A. Erdőhelyi, *Catalysts* **2020**, *10*, 155.
[38] K. Zhao, L. Wang, M. Calizzi, E. Moioli, A. Züttel, *J. Phys. Chem. C* **2018**, *122*, 20888–20893.
[39] A. Efremova, T. Rajkumar, Á. Szamosvölgyi, A. Sápi, K. Baán, I. Szenti, J. Gómez-Pérez, G. Varga, J. Kiss, G. Halasi, Á. Kukovecz, Z. Kónya, *J. Phys. Chem. C* **2021**, *125*, 7130–7141.
[40] J. Raskó, T. Kecskés, J. Kiss, *J. Catal.* **2004**, *226*, 183–191.
[41] G. Rupprechter, T. Dellwig, H. Unterhalt, H. J. Freund, *J. Phys. Chem. B* **2001**, *105*, 3797–3802.
[42] A. Sápi, G. Halasi, J. Kiss, D. G. Dobó, K. L. Juhász, V. J. Kolcsár, Z. Ferencz, G. Vári, V. Matolin, A. Erdöhelyi, Á. Kukovecz, Z. Kónya, *J. Phys. Chem. C* **2018**, *122*, 5553–5565.
[43] L. Zhang, J. Yu, X. Sun, J. Sun, *J. CO2 Util.* **2023**, *71*, 102460.
[44] T. Pu, W. Zhang, M. Zhu, *Angew. Chem. Int. Ed.* **2023**, *62*, e202212278.
[45] M. Yadav, I. Szenti, M. Ábel, Á. Szamosvölgyi, K. B. Ábrahámné, J. Kiss, P. Zsolt, A. Sápi, Á. Kukovecz, Z. Kónya, *ChemCatChem* **2023**, *15*, e202200717.
[46] C. Lentz, S. P. Jand, J. Melke, C. Roth, P. Kaghazchi, *J. Mol. Catal. A* **2017**, *426*, 1–9.
[47] Y. Wang, H. Arandiyan, J. Scott, K. F. Aguey-Zinsou, R. Amal, *ACS Appl. Energ. Mater.* **2018**, *1*, 6781–6789.
[48] L. Óvári, J. Kiss, *Appl. Surf. Sci.* **2006**, *252*, 8624–8629.
[49] S. Lee, C. Lin, S. Kim, X. Mao, T. Kim, S. J. Kim, R. J. Gorte, W. Jung, *ACS Catal.* **2021**, *11*, 13935–13946.
[50] X. Li, Q. Hu, H. Wang, M. Chen, X. Hao, Y. Ma, J. Liu, K. Tang, A. Abudula, G. Guan, *Appl. Catal. B* **2021**, *292*, 120172.
[51] Z. H. Qin, M. Lewandowski, Y. N. Sun, S. Shaikhutdinov, H. J. Freund, *J. Phys. Condens. Matter* **2009**, *21*, 134019.

Manuscript received: November 14, 2023
Accepted manuscript online: December 20, 2023
Version of record online: January 10, 2024